Journal of Materials Chemistry A

Solvent-assisted Structural Phase Transition of Zn-MOF from 2D to 3D and its Microflower Superstructural Carbon for Supercapacitors

Journal:	*Journal of Materials Chemistry A*
Manuscript ID	TA-ART-02-2025-001165.R1
Article Type:	Paper
Date Submitted by the Author:	14-Apr-2025
Complete List of Authors:	Wang, Min-Xian; Hangzhou Normal University, Key Laboratory of Organosilicon Chemistry and Material Technology of Ministry of Education Kim, Minjun; University of Queensland Iqbal, Muhammad; Institut Teknologi Bandung Zhang, Fei-Bao; Hangzhou Normal University, Key Laboratory of Organosilicon Chemistry and Material Technology of Ministry of Education Yamauchi, Yusuke; University of Queensland, Chemical Engineering; Nagoya University,

Solvent-assisted Structural Phase Transition of Zn-MOF from 2D to 3D and its Microflower Superstructural Carbon for Supercapacitors

Min-Xian Wang[a], Minjun Kim[b]*, Muhammad Iqbal[c,d], Fei-Bao Zhang[a]*, Yusuke Yamauchi[b, e, f]

[a]Key Laboratory of Organosilicon Chemistry and Material Technology of Ministry of Education, College of Material, Chemistry and Chemical Engineering, Hangzhou Normal University, Hangzhou 310012, China.

[b]Australian Institute for Bioengineering and Nanotechnology (AIBN), The University of Queensland, Brisbane, QLD 4072, Australia.

[c]Advanced Functional Materials Laboratory, Faculty of Industrial Technology, Institut Teknologi Bandung, Bandung 40132, Indonesia.

[d]Research Center for Nanosciences and Nanotechnology, Institut Teknologi Bandung, Bandung 40132, Indonesia.

[e]Department of Materials Process Engineering, Graduate School of Engineering, Nagoya University, Nagoya, Aichi 464-8603, Japan.

[f]Department of Chemical and Biomolecular Engineering, Yonsei University, Seoul 03722, Republic of Korea.

Emails: minjun.kim@uq.edu.au; feibaozhang@hznu.edu.cn

Abstract

Green synthesis of two-dimensional metal-organic frameworks (2D MOFs) and their further modifications to hierarchical structures are of great interest in achieving sustainable and high-performing energy storage devices. However, the synthesis of 2D MOFs often accompanies complicated synthetic methods requiring modulators (*e.g.*, templates and surfactants) or the interfacial growth strategy for anisotropic MOF growth. Moreover, 2D MOFs are prone to aggregation and restacking, thus losing accessible surface area and achieving only a limited performance for target applications. To address such challenges, this study demonstrates a recrystallization-guided structural phase transition of 2D MOF nanosheets to superstructural three-dimensional (3D) MOF exhibiting a flower-like morphology. This synthesis strategy is highly sustainable as it effectively omits the use of harmful modulators, allowing significantly reduced contamination with simpler separation processes. Besides, it also adds the versatility of MOFs in achieving various morphologies which is a critical aspect of control in obtaining greater capacity and durability for electrochemical applications. After carbonization, the microflower superstructural morphology 3D MOF is well retained with abundant active sites and hierarchical distribution of nanopores, enhancing electrolyte ion transport and demonstrating excellent performance as electrode materials for supercapacitors.

Keywords: Solvent effect; Structural phase transition; Ultrathin nanosheets; Microflower; Porous carbon; Supercapacitors

1. Introduction

With an alarming global awareness to avoid the use of toxic chemicals, the research on green synthesis of materials has become inevitable in today's hyperconnected society requiring an ever-increasing supply of advanced materials. In this context, a relatively recent type of porous crystalline materials known as metal-organic frameworks (MOFs) have demonstrated their usefulness in various applications, including sensing, electrochemical energy conversion, electrochemical energy storage, and catalysis.[1-7]

Among them, 2D MOFs are known to exhibit unique features of abundant exposed active sites, short diffusion pathways for electrolytes, and superior electrical conductivity for the applications.[8-9] Their ultrathin, porous, and crystalline frameworks of coordinated organic linkers and metal nodes can be effectively synthesized by top-down and bottom-up strategies, which include ultrasonic stripping, lyophilization stripping, interface synthesis, surfactant-assisted synthesis, modulated synthesis, *etc*.[10, 11] However, their 2D nature accompanies common structural limitations, including the loss of accessible surface area and active sites due to restacking and low electrochemical stability due to disproportionate chemical activity in their structure with edge sites being generally more active than basal planes.

To avoid such structural limitations of 2D MOFs, a concept of nanoarchitecturing is generally implemented in materials synthesis. For instance, Duan *et al.* reported *in situ* growth strategy to induce a vertical growth of ultrathin 2D MOF nanosheet in the form of arrays on Ni foam.[12] This strategy effectively enhances the spatial separation of 2D MOF nanosheets, thus improving the catalytic activity for oxygen evolution reaction with more accessible active sites. Alternatively, Ran *et al*. demonstrated *in situ* interpenetration method to successfully integrate carbon nanotubes with carboxylate functional groups (C-CNTs) and ultrathin Ni-MOFs to avoid loss of active sites and electrochemical performance.[13] More recently, Song *et al.* utilized an ice-templating strategy to fabricate 2D layered MOF superstructures.[14] In their strategy, individual MOF nanoparticles are forced by ice crystals to self-assemble into 2D superstructures with controllable number of layers. Since the resulting 2D layered MOF superstructures consist of numerous MOF nanoparticles, the restacking effect is significantly reduced due to the presence of interparticle space and relatively bumpier surface.

In addition to these methods, a recrystallization reaction has emerged as a powerful nanoarchitecturing approach.[15-17] The strategy stems from the fact that weak coordination bonds between organic linkers and metal nodes in MOFs are susceptible to repeated bond breaking and forming under a specific condition (*e.g.*, at high pressures and/or temperatures, the presence of additives, altered pH, *etc*.). Through repeated bond breaking and forming, dissolution-recrystallization process occurs to induce the growth of altered unit cell

structures with or without preferred orientations for further nanoarchitecturing.

The recrystallization strategy can be further refined using other crystal engineering methods (*e.g.*, coordination modulation synthesis, protonation/deprotonation method, and surfactants/capping agents' modulation), to extend the nucleation phase through competitive coordination of the metal nodes, lowering solution pH to inhibit ligand deprotonation or adsorption of amphiphiles on special crystal facets.[18-20] As the prolonged nucleation phase is associated with the increased number of smaller MOF crystals, MOF recrystallization with alternative crystal engineering holds a great potential for developing superstructures. However, the use of additives not only compromises the green synthesis of materials but also may serve as a new ligand component or capping agent, leading to uncertain impacts on the overall physicochemical properties of products.[21, 22]

Generally, different solvents are known to affect the nucleation and growth of MOFs depending on their compositions, physical and chemical properties [*e.g.*, hard and soft acids and bases (HSAB) theory, polarity, ability to form hydrogen bonds], and volume (precursor concentration). In addition, some insights have revealed that the solvent can serve as a weak ligand in frameworks and also as a surfactant to preferentially adsorb on the crystal surfaces to accelerate or inhibit the growth of crystal faces, resulting in abundant morphology.[23-25] As our previous studies demonstrated that alcohols (amphiphilic molecules) can perform a dual role of facet-masking agent and modulator, we present a simple and green synthetic strategy for 2D MOFs and their recrystallized microflower superstructure using only alcohol molecules as the solvent and modulator.[4, 26]

Herein, this work presents the solvent-assisted structural phase transition strategy to obtain microflower superstructural Zn-based MOF (Zn-MOF). The effect of the carbon chain length of alcohol on the formation of microflower superstructure *via* the recrystallization process is stipulated, and various structures (*e.g.*, microflowers, cellular particles, and lamellar structures) can be derived by different alcohol species. The study demonstrates that the HSAB theory is responsible for the successful recrystallization to microflower superstructure. 2D Zn-MOF precursor (Zn-BDC-NH_2 denoted as P-ZBN) was successfully recrystallized in methanol (CH_3OH) to the microflower superstructure (ZBN-M), which was finally converted to its carbonaceous form (ZBN-M-900) by a direct-carbonization process at 900 ºC. With a combined effect between the recrystallized microflower superstructure and enhanced nanoporosity, ZBN-M-900 serves as a high-performance supercapacitor electrode material. Specifically, the microflower superstructures effectively provide larger reservoir and contact area for the electrolyte ions, thus improving the adsorption speed and the transmission of electrolyte ions. Given this, ZBN-M-900 demonstrates good rate capacity and high energy density performance in a symmetric supercapacitor device.

2. Results and discussion

2.1. Preparation and characterization of Zn-based MOFs

Microflower superstructural Zn-based MOFs (ZBN-M) were synthesized *via* a simple two-step method as shown in Fig. 1a. In a typical synthesis, the Zn-BDC-NH_2 precursor (P-ZBN) was initially prepared by mixing 2-aminoterephthalic acid (BDC-NH_2) and Zn acetate dihydrate in CH_3OH and sonicating the solution for half an hour. Subsequently, P-ZBN was subjected to solvothermal treatment in CH_3OH at 130 ºC to induce a partial dissolution of P-ZBN and a following recrystallization to form highly homogeneous flower-like structures (denoted as ZBN-M). The as-prepared P-ZBN has an irregular flake structure with a mean diameter of 0.50 μm and a thickness of around 3.50 nm as determined by the scanning electron microscope (SEM) and atomic force microscope (AFM), respectively (Fig. 1b and Fig. S1). After the solvothermal treatment, P-ZBN successfully transforms into ZBN-M. The SEM and transmission electron microscope (TEM) images of ZBN-M demonstrate a mean diameter of 2.17 μm with exposed surface and internal structure consisting of highly interlaced nanosheets (Fig. 1c-g and Fig. S2). The elemental mapping of ZBN-M reveals that carbon, nitrogen, oxygen and zinc atoms are homogeneously distributed throughout the structure, indicating that the recrystallization process occurs homogenously (Fig. 1h).

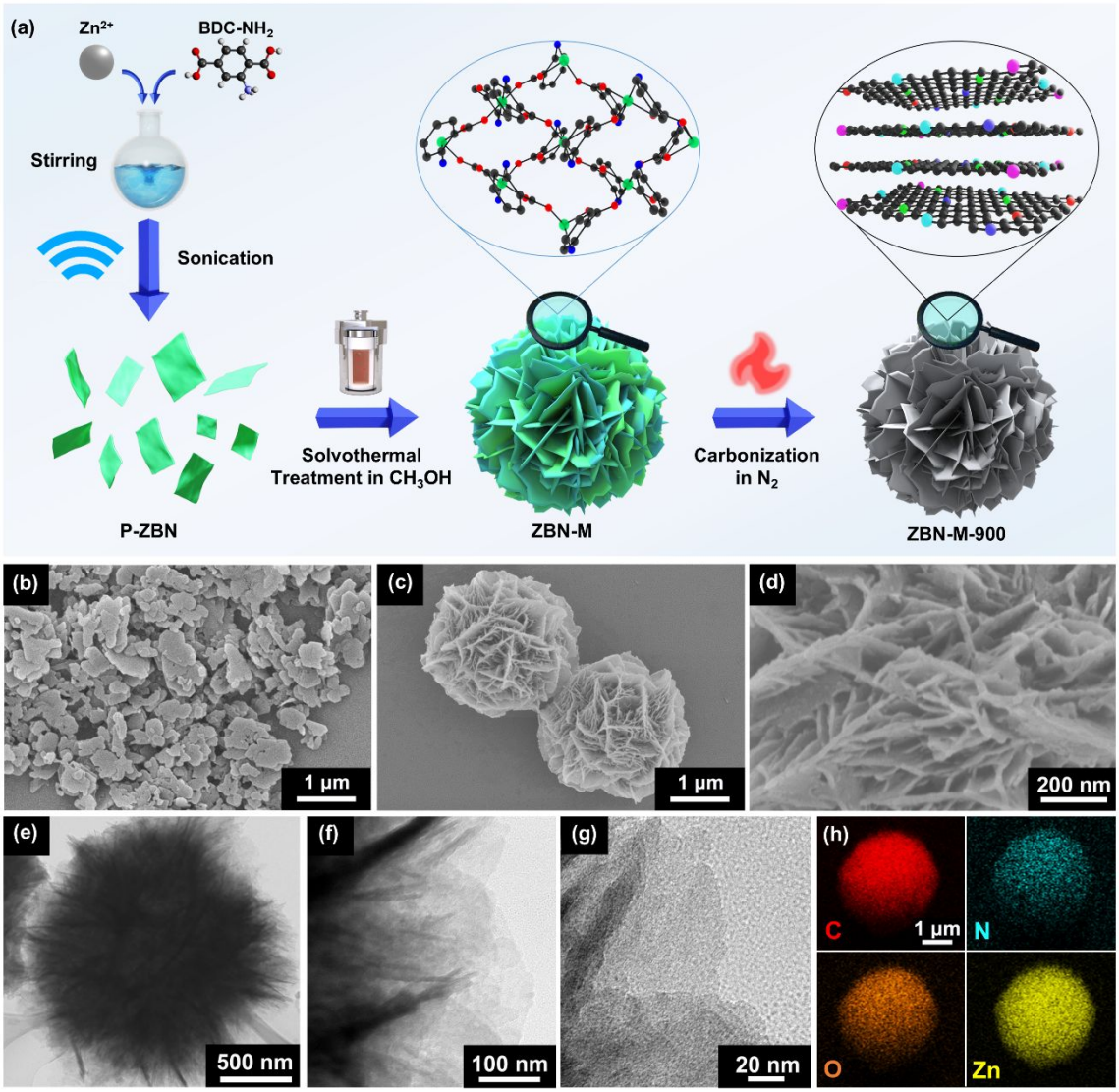

Fig. 1 (a) Schematic description for the preparation of flower-like Zn-based MOFs and derivates. SEM images of (a) P-ZBN, (c-d) ZBN-M. (e-g) TEM images and (h) EDS-elemental mapping of ZBN-M.

Based on the nitrogen sorption isotherms, specific surface area calculated by Brunauer–Emmett–Teller (BET) method (S_{BET}) for ZBN-M is 71.6 m^2 g^{-1}, which is 4.16 times greater than that of P-ZBN (17.2 m^2 g^{-1}), thus demonstrating the benefit of morphological transformation to flower-like structure to prevent serious restacking of pristine nanosheet structure (Fig. S3). As can be envisaged from morphology, ZBN-M has a significantly greater uptake of nitrogen at high P/P_0 above 0.8 due to their large interparticle space between interlaced nanosheets.[27] In addition to Fourier transform infrared spectroscopy (FTIR) analysis (Fig. S4), X-ray photoelectron spectroscopy (XPS) analysis was performed. From XPS analysis, Zn, C, N, and O atoms are identified in ZBN-M (Fig. S5a). The deconvolution of the C 1 s spectrum presents three peaks at 284.7, 285.7, and 288.6 eV, which were assigned to the C-C, C-N, and C=O bonds of ZBN-M, respectively (Fig. S5b).[28] The N 1s spectrum was deconvoluted into two superimposed peaks at 399.4 eV and 400.4 eV,

corresponding to the free amine and coordinated amine groups, respectively (Fig. S5c).[29]

2.2. Mechanistic study of the formation process of ZBN-M

To explore the mechanism behind the formation of ZBN-M, a series of experiments were carried out for various parameters such as solvent type, reaction time and temperature. First, the change in the crystal structure of P-ZBN to ZBN-M depending on the solvothermal reaction time was studied by X-ray diffraction (XRD) analysis. Based on the XRD spectra, the diffraction peaks of P-ZBN match well with the simulated diffraction patterns of Zn-BDC-NH_2 (CCDC Number: 607821) (Fig. 2a-i and 2-iii).[30] As P-ZBN undergoes the solvothermal reaction in CH_3OH at 130 ºC, its crystal structure gradually shifts to alternative form of Zn-BDC-NH_2 (CCDC Number: 1943053) (Fig. 2a-ii).[31, 32] Specifically, after 1 hour of the solvothermal reaction, a mixed diffraction pattern involving peaks for both types of Zn-BDC-NH_2 is observed, indicating the occurrence of dissolution-recrystallization process (Fig. 2a-iv). After 3.5 hours, the diffraction peaks for Zn-BDC-NH_2 (CCDC Number: 607821) disappear while that of Zn-BDC-NH_2 (CCDC Number: 1943053) become broadened, especially for the (4 0 0) and (1 1 1) crystallographic planes, potentially due to the nanocrystalline nature of ZBN-M (Fig. 2a-v and 2a-vi).

Based on the HSAB theory, MOFs that are formed by the weak coordination bond between Zn^{2+} (borderline Lewis acid) and carboxylate linkers (hard Lewis acids) are not chemically stable, hence more susceptible toward the reconstruction of their crystal structure into *via* bond breaking and reforming.[26, 33] Specifically, P-ZBN exhibits a monoclinic system with $P2_1/c$ space group with Zn(II) centers displaying a distorted $ZnNO_5$ octahedral geometry, where the equatorial sites are occupied by two water molecules and other sites by either amine group or bidentate carboxylate group (Fig. 2b). As a type of amphiphilic molecule, CH_3OH can diffuse and adsorb to the internal surface of P-ZBN. During its diffusion, CH_3OH undergoes a deprotonation to CH_3O^-, making the local environment a weakly acidic and inducing the oscillations of Zn–O bonds around the Zn–Zn node.[34] Then, the as-formed CH_3O^- can serve as a Lewis base to disrupt the weak metal-ligand bond (Zn-O) and coordinate with the Zn-O octahedral cluster, triggering the ligand exchange with H_2O and BDC-NH_2^{2-}. Under solvothermal conditions, this ligand exchange facilitates the structure collapse and dissolution of the precursor. Meanwhile, the solubility of polar BDC-NH_2^{2-} decreases as its concentration increases to reduce the polarity of the solvent and tends to re-coordinate with Zn(II) center and form O-Zn-N tetrahedral coordination and transform into alternative monoclinic system with *Cc* space group. This dissolution-recrystallization with the repeating ligand exchange process induces the transformation of P-ZBM to ZBN-M with and ZBN-M nucleation and growth on the surface of P-ZBN. Based on the refined XRD spectra, a

structural phase transition from $P2_1/c$ space group (CCDC Number: 607821) to Cc space group (CCDC Number: 1943053) is observed upon the prolonged solvothermal reaction in CH_3OH (Fig. S6a-d). Specifically, 99.71% of $P2_1/c$ space group and 0.29% of Cc space group in P-ZBN undergo the structural phase transition 99.84% of Cc space group and 0.16% of $P2_1/c$ space group in ZBN-M (Fig. S6e). Along with the phase transition in crystal structures during the solvothermal treatment in CH_3OH, the morphological evolution of ZBN-M is confirmed by SEM images. It is observed that P-ZBN first undergoes dissolution to form irregular spherical aggregates after 0.5 h of solvothermal treatment in CH_3OH (Fig. S7). It then transforms into an initial flower-like structure after 1.5 h (Fig. 2c and 2d), which further evolves to the primary microflower superstructure after 6 hours (Fig. 2e and 2f). Next, the effect of solvothermal reaction temperatures on the morphological evolution of ZBN-M were investigated. Though no obvious morphological change from that of P-ZBN is observed at a relatively low temperature of 90 ℃, the microflower superstructure appears at elevated temperatures from 110 ℃ (Fig. 2g-i and g-ii). At 130 ℃, highly spherical and homogeneous microflower superstructure is achieved by ZBN-M (Fig. 2g-iii). Further increase in temperature to 150 ℃ results in the morphological distortion, favoring an anisotropic crystal growth (Fig. 2g-iv).

To broaden the understanding behind the successful formation of microflower superstructure, we then investigated the effect of different solvents in the dissolution-recrystallization of P-ZBN as it can affect the coordination interaction of metal nodes and organic ligands during solvothermal reactions. With typical aprotic solvents (DMF, acetone and toluene) or water as a typical protic solvent for the solvothermal reactions at 130 ℃, the desired microflower superstructure of ZBN-M is not achieved (Fig. S8). Furthermore, the length of nonpolar carbon chain of alcohol is also found to influence morphological evolution during the solvothermal reaction. Specifically, methanol (CH_3OH), ethanol (C_2H_5OH), 1-propanol (C_3H_7OH), butyl alcohol (C_4H_9OH), hexyl alcohol ($C_6H_{13}OH$), 1-octanol ($C_8H_{17}OH$) and 1-decanol ($C_{10}H_{21}OH$) were implemented and their resulting solvothermal products are presented by the SEM images (Fig. 2h). Interestingly, only CH_3OH successfully produced microflower superstructure (Fig. 2g-iii) while the products of other alcohol solvents demonstrate a foliated structure at a varied degree depending on the length of nonpolar carbon chain (Fig. 2h). It is inferred that the morphological change of the respective product is caused as the solubility of the polar BDC-NH_2 tends to increase as the length of nonpolar carbon chain decreases in the order of $C_{10}H_{21}OH < C_8H_{17}OH < C_6H_{13}OH < C_4H_9OH < C_3H_7OH < C_2H_5OH < CH_3OH$.[32]

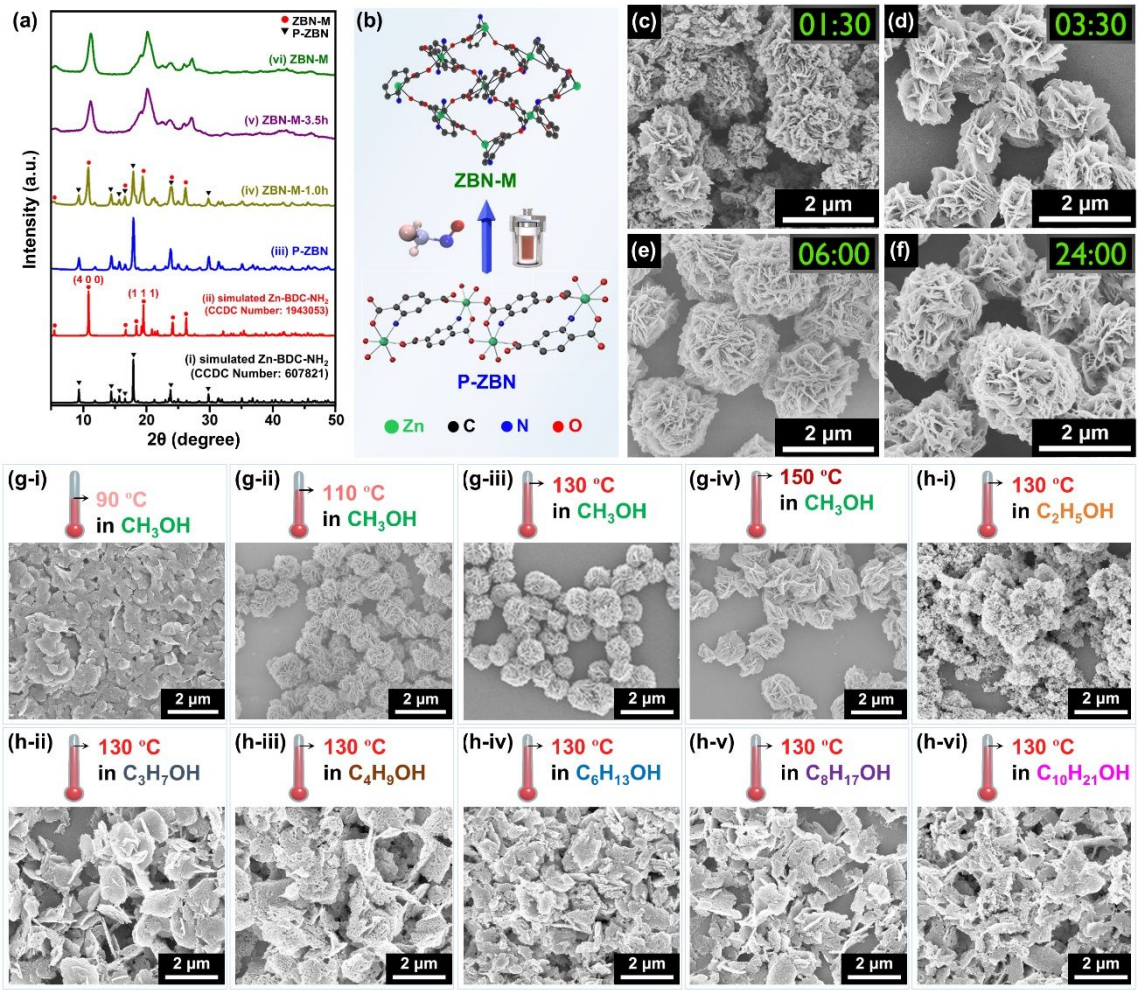

Fig. 2 The simulated XRD patterns for Zn-BDC-NH_2 from CCDC Number: (a-i) 607821 and (a-ii) 1943053. The measured XRD patterns for (a-iii) P-ZBN, (a-iv) ZBN-M-1.0h, (a-v) ZBN-M-3.5h and (a-vi) ZBN-M. (b) Schematic description of recrystallization process with simulated crystal structures of P-ZBN to ZBN-M. SEM images of ZBN-M synthesized in methanol at 130 ℃ for (c) 1.5 h, (d) 3.5 h, (e) 6.0 h and (f) 24 hr. SEM images of ZBN-M synthesized in methanol at (g-i) 90 ℃, (g-ii) 110 ℃, (g-iii) 130 ℃ and (g-iv) 150 ℃. SEM images of solvothermal products synthesized in (h-i) C_2H_5OH, (h-ii) C_3H_7OH, (h-iii) C_4H_9OH, (h-iv) $C_6H_{13}OH$, (h-v) $C_8H_{17}OH$ and (h-vi) $C_{10}H_{21}OH$.

2.3. Preparation of microflower superstructural carbon derived from ZBN-M

Since MOFs are commonly subjected to a pyrolysis process to obtain MOF-derived porous carbons which have high porosity and large surface area, we further investigated the thermal conversion of ZBN-M to its carbonaceous forms and their potential as an electrode material for supercapacitors. Though carbon materials derived from 2D MOFs are expected to offer advantages such as greater structural flexibility, good electrical conductivity, and exposed surface-active sites, they are increasingly more susceptible to restacking due to the anisotropic nature with high interfacial adhesion energy.[35] The microflower superstructure of ZBN-M

obtained through recrystallization process, on the other hand, exhibits highly foliated 2D MOF nanosheets assembled into a single particle, thus potentially reducing the restacking effect and benefit as a supercapacitor electrode material. Herein, ZBN-M was carbonized directly at 900 ºC under N_2 atmosphere to synthesize its carbonaceous form doped with nitrogen heteroatoms (denoted as ZBN-M-900) (Fig. 3a).

From the SEM image, ZBN-M-900 successfully inherits the microflower superstructure of its precursor ZBN-M (Fig. 3b and Fig. 3c). However, its mean diameter is 1.00 μm which is smaller than that of its precursor ZBN-M (2.17 μm) (Fig. S2 and S9). Such reduction in the size of carbon particle is potentially due to the thermal shrinkage of the structure caused by the decomposing BDC-NH_2 linkers and evaporating Zn atoms at a high annealing temperature of 900 ºC.[36] TEM images of ZBN-M-900 indicate the formation of hollow center covered by ultrathin amorphous carbon nanosheets with abundant micropores (Fig. 3d-f). From elemental mapping, it is clear that ZBN-M-900 is heteroatom-doped with N and O atoms throughout its structure (Fig. 3g). Based on the thermogravimetric analysis, specific stages involved in the carbonization process of ZBN-M are better elucidated (Fig. S12). An initial slight decrease in the weight to 96.80% at 81.1 ºC is mostly caused by the removal of adsorbed water molecules in the pores. In the temperature range between 311.1 ºC and 498.5 ºC, a substantial decrease in the weight of 54.10% is noted. Such dramatic weight loss is caused by the thermal decomposition of BDC-NH_2 linkers. The following loss of 6.61% from 498.5 ºC and 699.9 ºC can be assigned to the continued decomposition of remaining BDC-NH_2 linkers and thermal evaporation of Zn atoms at such elevated annealing temperatures. Overall, there is a total weight loss of 66.63% at 1000 ºC, indicating a clear collapse and rearrangement of ZBN-M to shrink its size.

In addition, various ZBN-M-*x* (where *x* denotes the carbonization temperature at 800, 850, 900, 950 and 1000 ºC) were prepared at different carbonization temperatures to understand the effect of carbonization temperature on the morphological changes. Their SEM images demonstrate similar microflower nanoarchitecture despite being subjected to different carbonization temperatures (Fig. S14). In terms of carbon microstructure, they are highly amorphous in nature as their XRD spectra exhibit only a broad peak at ~25º corresponding to (0 0 2) lattice plane of graphite appears (Fig. S15a). As the level of graphitization of carbon materials can be inferred by the intensity ratio between D and G bands (I_D/I_G) in the Raman spectrum, I_D/I_G values of ZBN-M-*x* were obtained.[35, 36] Their I_D/I_G values corroborate diffraction pattern and further confirm their amorphous nature (Fig. S15b).

According to the physisorption behavior for N_2 in an isothermal condition, porous structures of ZBN-M-*x* are highly hierarchical in nature consisting of micro- meso- and macropores. Specifically, the isotherms of ZBN-M-*x* (*x* = 800, 850, 900, 950 and 1000) exhibit large initial N_2 uptake volume at P/P_0 below 0.05, indicating

the presence of abundant micropores (Fig. 3h and Fig. S16). The physisorption behavior of ZBN-M-*x* well reflects the morphological observation as evidenced by an exceptional increase in their S_{BET} (above 1000 m^2 g^{-1}) from that of its precursor ZBN-M achieving S_{BET} value of only 71.6 m^2 g^{-1}, largely due to the formation of additional micropores by thermal decomposition of BDC-NH_2 linkers and evaporating Zn atoms passing through the carbon matrix.[36]

After carbonization, a noticeable decrease in the amount of heteroatom N and O is observed for ZBN-M-900 as compared to its precursor ZBN-M (Fig. S5 and Fig. S13) mainly due to the thermal decomposition and oxidation of the BDC-NH_2 ligand. From the deconvoluted high-resolution XPS spectra for C 1s and N 1s of ZBN-M-900, it is noted that the carbon matrix involves pyridinic-N (398.3 eV), pyrrolic-N (399.6 eV), and graphitic-N (401.0 eV), which are known to be beneficial for electrode materials for supercapacitors as they contribute to increase the wettability and electrical conductivity (Fig. 3i and 3j).[37-39]

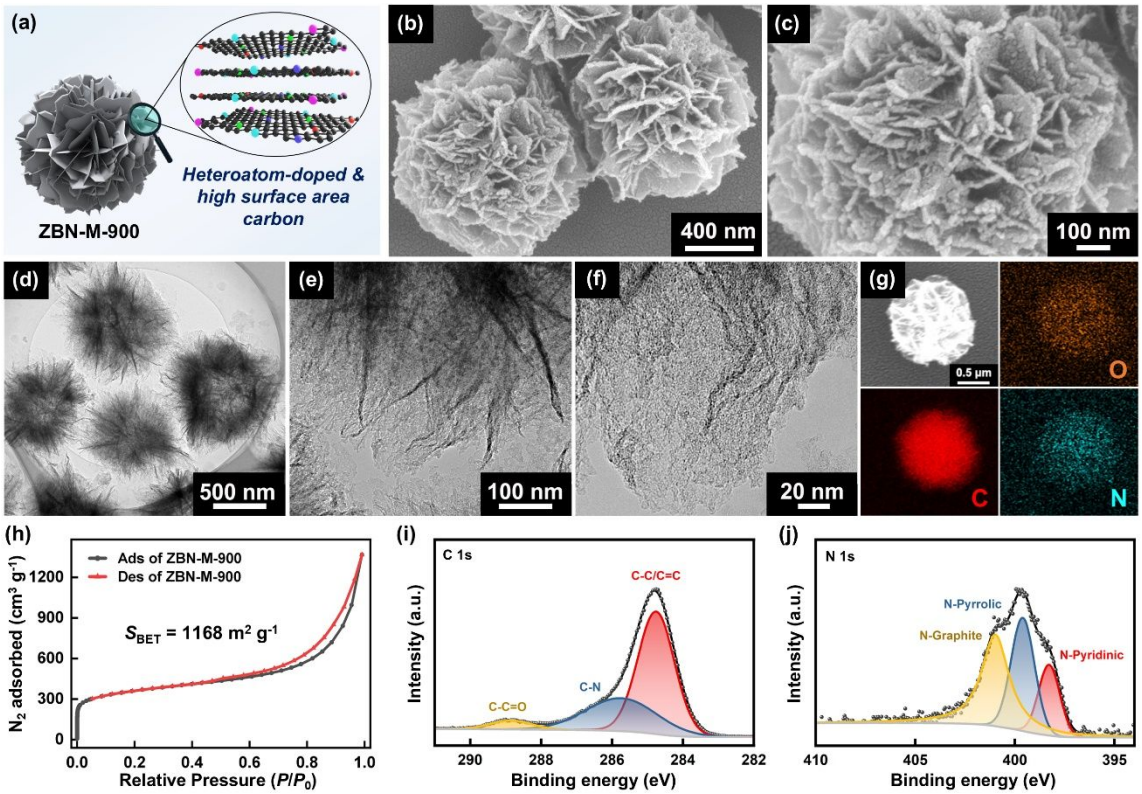

Fig. 3. (a) Schematic description of microflower superstructure and carbon matrix with heteroatoms of ZBN-M-900. (b, c) SEM images of ZBN-M-900. (d-f) TEM images of ZBN-M-900. (g) EDS mapping of ZBN-M-900. (h) N_2 adsorption/desorption isotherms of ZBN-M-900. High-resolution XPS spectra of ZBN-M-900 for (i) C 1s and (j) N 1s.

2.4. Electrochemical analysis of microflower superstructural carbon derived from ZBN-M

The electrochemical performance of ZBN-M-900 were first investigated in 1.0 M H_2SO_4, 1.0 M Na_2SO_4, and 1.0 M KOH by cyclic voltammetry (CV) and galvanostatic charge-discharge (GCD) to evaluate the electrolyte effect on the specific capacitance. As shown in Fig. S17, the highest specific capacitance of samples calculated from the GCD measurement are 292 F g^{-1} in 1.0 M H_2SO_4, 118 F g^{-1} in 1.0 M Na_2SO_4 and 186 F g^{-1} and 1.0 M KOH, which may be attributed to the hydrated ionic radius, ionic mobility, and molar ionic conductivity of the three electrolytes.[40, 41] Next, the influence of carbonization temperature on the electrochemical performance was studied with ZBN-M-*x* obtained at different carbonization temperatures (*i.e.*, 800, 850, 900, 950 and 1000 ºC) in 1.0 M H_2SO_4 (Fig. S18). Among ZBN-M-*x*, ZBN-M-900 achieves the largest area and the longest charge-discharge time in the CV and GCD curves, respectively, indicating that it successfully generates greater specific capacitance than others synthesized at varied temperatures from 800 to 1000 °C. Furthermore, ZBN-M-900 is found to outperform specific capacitance of other carbon materials obtained at 900 °C whose precursors were synthesized by varying solvothermal conditions (*e.g.*, type of solvent, temperature and time), therefore successfully highlighting the advantage of hierarchical microflower structures to enhance ionic migration through the electrode (Fig. S19).[42]

With this, more in-depth electrochemical analysis was conducted for ZBN-M-900 by CV, GCD, and electrochemical impedance spectroscopy (EIS) in 1.0 M H_2SO_4. As shown in Fig. 4a, the CV curves of ZBN-M-900 display typical quasi-rectangular shapes with reversible redox peaks between 0.2 and 0.4 V at various scan rates from 1 to 20 mV s^{-1}. The redox peaks may be ascribed to the reduction/oxidation of quinone-type oxygen, contributing to a certain level of pseudocapacitance to exhibit a hybrid energy storage mechanism.[43-45] To get further insight for the energy storage behavior of ZBN-M-900, CV curves were further analyzed to distinguish the relative contributions of a diffusion-controlled process and a surface adsorption-controlled process by calculating *b*-values based on the following equation: $i = av^b$, where *i* is the peak current intensity, *v* is the scan rate, *a* and *b* are adjustable constants.[26] The anodic and cathodic *b*-values are 0.95 and 0.90, respectively, from which it can be inferred that the energy storage behavior of ZBN-M-900 is mainly contributed by the surface-controlled adsorption process. The relative proportion of typical capacitive contribution to total energy storage capacity can be determined by following equation: $i(V) = k_1v + k_1v^{1/2}$, where *i* is the total current intensity and k_1v and $k_1v^{1/2}$ reflect the capacitive and diffusion-controlled charge storage, respectively.[45] As shown in Fig. 4d, the capacitive proportion increases with the scan rate, revealing that the capacitive behavior dominates the total capacitance of the ZBN-M-900 electrode at high scan rates. Though the electro-oxidation of N species in the carbon matrix is expected to contribute to the pseudocapacitance behavior, the high-temperature annealing process causes the breaking of C-N bonds and

form NO_x (C-C: 370 kJ mol^{-1}; C-N: 305 kJ mol^{-1}).[46] Therefore, only a limited content of N species remains doped in ZBN-M-900, leading to low diffusion-controlled charge storage.

The GCD curves of ZBN-M-900 (Fig. 4e) present nearly symmetrical triangular-like profiles with comparable charge and discharge times, indicating excellent coulombic efficiency.[47] According to the GCD curves, the specific capacitance values at 0.5, 1, 2, 3, 4, 5, and 10 A g^{-1} are 308.25, 292.4, 275.2, 267, 261.2, 257, and 243 F g^{-1}, respectively (Fig. 4f). To offer more extensive comparison in the effect of nanoarchitecture on electrochemical performance, IRMOF-3-derived carbon obtained at 900 ºC (IRMOF-3-900), exhibiting a bulk morphology in the micrometer scale, was synthesized (Fig. S20a-d).[48] Specifically, IRMOF-3-900 achieves specific capacitance of 227, 215, 196, 189, 184, 178, and 166 F g^{-1} at 0.5, 1, 2, 3, 4, 5, and 10 A g^{-1}, respectively, which are significantly lower than that of ZBN-M-900 at the corresponding current density (Fig. S20e-g). Due to the unique microflower-like structures with hierarchical porous structures, leading to rapid ion diffusion/storage behavior, ZBN-M-900 presents good rate capability at high current density.[49]

According to the EIS analysis, the Nyquist plot of ZBN-M-900 presents a quasi-vertical line in the low-frequency region, indicating nearly ideal capacitive properties (Fig. 4g). The calculated equivalent series resistance (R_S) and charge transfer resistance (R_{CT}) are 0.84 Ω and 0.29 Ω, respectively, demonstrating a good conductivity of the ZBN-M-900 electrode. The cycle life of active materials was evaluated with the GCD test for 10000 cycles at 10 A g^{-1} and shown in Fig. 4h. The specific capacitance retention rate of the ZBN-M-900 electrode material is 98.46% after the test cycles, indicating extraordinary charge-discharge reversibility. This was confirmed by SEM images (Fig. S21) and XRD analyses (Fig. S22) characterized before and after long-term cycles, showing that there are no significant changes in the active material after the long cycling process.

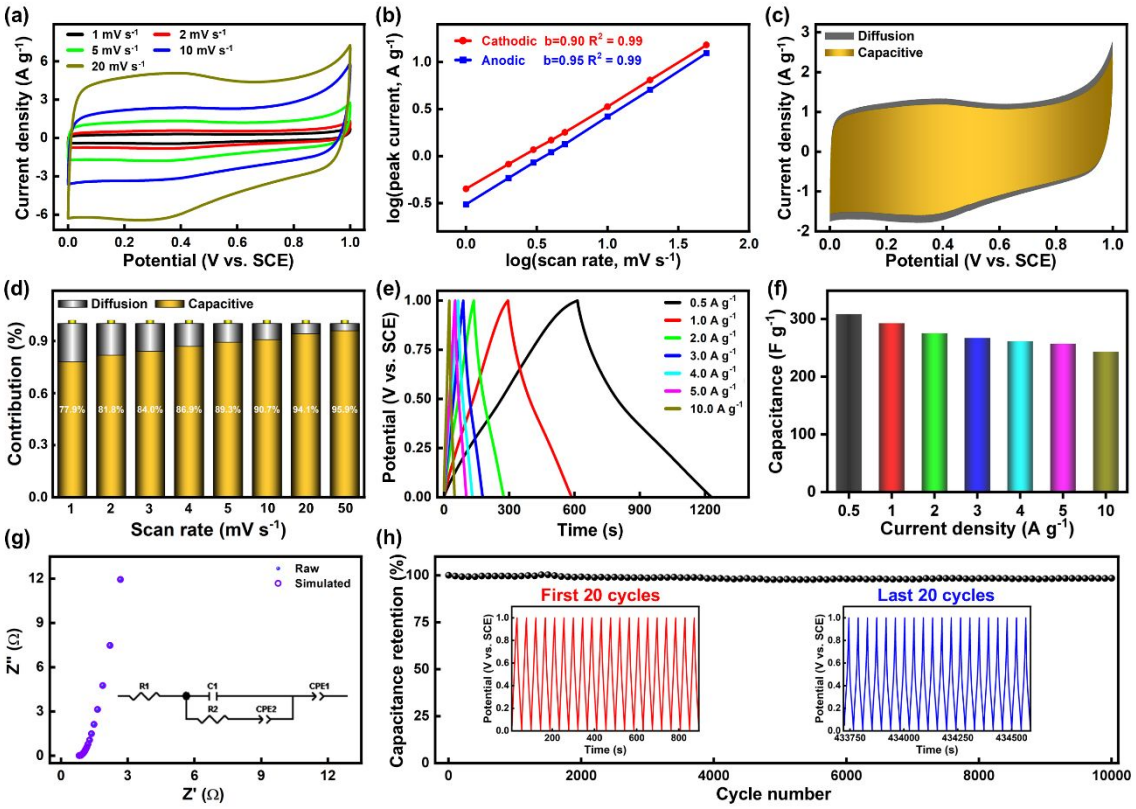

Fig. 4. Electrochemical performances of ZBN-M-900 in a three-electrode configurations using 1 M H_2SO. (a) CV curves at scan rates from 1 mV s^{-1} to 20 mV^{-1}. (b) Plots of the log *i* of the cathode and anodic peak versus the log *v*. (c) Capacitive and diffusion contribution ratio at a scan rate of 5 mV s^{-1}. (d) Comparison of diffusion and capacitive ratios at scan rates from 1 mV s^{-1} to 50 mV^{-1}. (e) GCD curves and (f) specific capacitances at varying current densities. (g) Nyquist plots and the equivalent circuit. (h) Cycle test at a current density of 10 A g^{-1} (Inset: the first and last 20 cycles of 10,000 cycles).

To investigate the practical application of ZBN-M-900, a symmetric supercapacitor (SSC) was fabricated with 1 M H_2SO_4 electrolyte. When the CV curves of ZBN-M-900 in SSC were measured at a scan rate of 10 mV s^{-1} in various potential windows from -0.4 V to 2.0 V, no distinct increment of anodic current is observed when the potential window is set between -0.4 V and 1.4 V (Fig. 5a). For the subsequent SSC evaluation, the potential window of -0.4 V to 1.4 V was therefore applied. At this voltage window, the quasi-rectangular shape is well maintained in CV curves at increasing scan rates from 1 mV s^{-1} to 100 mV s^{-1}, demonstrating the fast charge-discharge reversibility of the SSC (Fig. 5b). From the GCD curves of the SSC measured at different current densities from 0.5 A g^{-1} to 10 A g^{-1}, a reasonably symmetric shape between the charge and discharge curves is observed, indicating a nearly ideal capacitive behavior as in the three-electrode measurements (Fig. 5c). Next, the Ragone plots of the fabricated ZBN-M-900//ZBN-M-900 SSC are compared to relevant reported data (Fig. 5d). Specifically, it exhibits a high energy density of 43.29 Wh kg-

[1] with a power density of 449.98 W kg^{-1} at a current density of 0.5A g^{-1}, which is superior to some recently reported SSC devices.[49-54] ZBN-M-900//ZBN-M-900 SSC also demonstrates highly stable cycling performance with only 0.6% decrease in capacitance after 10000 charge-discharge processes (Fig. S23).

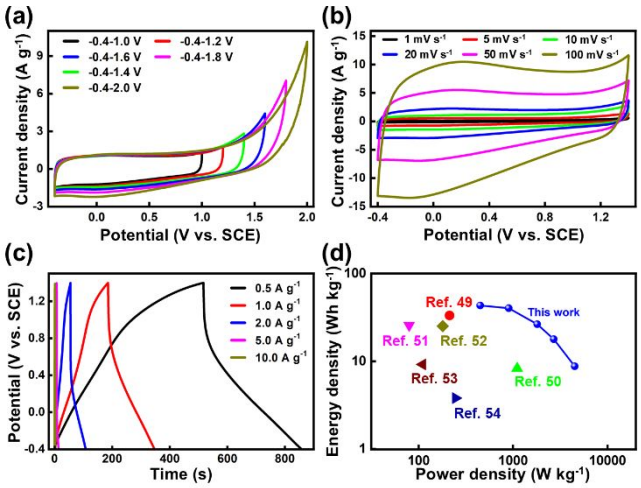

Fig. 5. Electrochemical performances of ZBN-M-900 for symmetric capacitors. (a) CV curves at various potential ranges. (b) CV curves and (c) GCD curves at different scan rates and current densities. (d) Ragone plots and reported other carbon-based SSC.

Conclusion

In summary, a solvent-assisted structural phase transition strategy successfully facilitates the morphological shift from 2D P-ZBN nanosheets to microflower superstructured ZBN-M *via* solvothermal dissolution-recrystallization in methanol. The as-synthesized microflower superstructured ZBN-M consists of numerous ultrathin nanosheets randomly arranged into microspheres. This work explicitly reveals that the morphological shift of P-ZBN *via* the solvent-assisted structural phase transition is highly dependent on solvothermal conditions (*e.g.*, solvent type, temperature, time). Due to the unique hierarchical superstructure, ZBN-M exhibits highly exposed surfaces with accessible active sites. Under carbonization conditions, the microflower superstructured ZBN-M undergo thermal conversion to its carbonaceous form that displays hierarchical porosity with abundant mesopores and macropores, thus further improving the surface area and activity sites for fast charge and ion transport and resulting in high capacitance. We envision that the present synthetic strategy for MOF nanoarchitecturing is potentially applicable to other types of MOFs to achieve novel morphologies and functionalities to benefit targeted applications.

Acknowledgement

This work was supported by the financial support from Hangzhou Normal University, the JST-ERATO Yamauchi Materials Space-Tectonics Project (JPMJER2003), the ARC Laureate Fellowship (FL230100095) and the UQ-Yonsei International Research Project. This work used the Queensland node of the NCRIS-enabled Australian National Fabrication Facility (ANFF). We demonstrate our appreciation for English editing software such as ChatGPT, Grammarly, *etc*.

References

1. X. Ren, Z. Liu, T. Zhang, X. Jiang, Q. Fang, Y. Li, F. Ma, R. Chen, H. Zhang, H. Ni, Review on two-dimensional metal–organic frameworks for biological sensing: current challenges and new frontiers, *J. Mater. Sci.* 59(24) (2024) 10724-10743.

2. R. Nivetha, S. Sharma, J. Jana, J.S. Chung, W.M. Choi, S.H. Hur, Recent Advances and New Challenges: Two-Dimensional Metal-Organic Framework and Their Composites/Derivatives for Electrochemical Energy Conversion and Storage, *Int. J. Energ. Res.* 2023 (2023) 8711034.

3. P. Priyadarshini, K. Parida, Two-dimensional metal-organic frameworks and their derived materials: Properties, synthesis and application in supercapacitors field, *J. Energy Storage* 87 (2024) 111379.

4. C.H. Wang, D.W. Zhang, S.D. Liu, Y. Yamauchi, F.B. Zhang, Y.V. Kaneti, Ultrathin nanosheet-assembled nickel-based metal-organic framework microflowers for supercapacitor applications, *Chem. Commun.* 58(7) (2022) 1009-1012.

5. M. Kim, K. K. Leong, N. Amiralian, Y. Bando, T. Ahamad, S. M. Alshehri, Y. Yamauchi, Nanoarchitectured MOF-derived porous carbons: Road to future carbon materials, *Appl. Phys. Rev.* 11 (2024) 041317.

6. J. Qi, Y. Yan, Y. Cai, J. Cao, J. Feng, Nanoarchitectured Design of Vertical-Standing Arrays for Supercapacitors: Progress, Challenges, and Perspectives, *Adv. Funct. Mater.* 31 (2021) 2006030.

7. Y. Yan, K. Bao, T. Liu, J. Cao, J. Feng, J. Qi, Minutes periodic wet chemistry engineering to turn bulk Co-Ni foam into hydroxide based nanosheets for efficient water decomposition, *Chem. Eng. J.* 401 (2020) 126092.

8. L. Wang, S.E. Saji, L. Wu, Z. Wang, Z. Chen, Y. Du, X.-f. Yu, H. Zhao, Z. Yin, Emerging Synthesis Strategies of 2D MOFs for Electrical Devices and Integrated Circuits, *Small* 18(33) (2022) 2201642.

9. Y. Han, C. Zhang, K.-J. Chen and T. Wang, *J. Mater. Chem. A* 12 (2024) 24296-24307.

10. Basree, A. Ali, K. Kumari, M. Ahmad, G.C. Nayak, Functional metal–organic frameworks derived electrode materials for electrochemical energy storage: a review, *Chem. Commun.* 60(91) (2024) 13292-13313.

11. J.J. Liu, G.L. Xing, L. Chen, 2D Conjugated Metal-Organic Frameworks: Defined Synthesis and Tailor-

Made Functions, *Acc. Chem. Res.* 57(7) (2024) 1032-1045.
12. J. Duan, S. Chen, C. Zhao, Ultrathin metal-organic framework array for efficient electrocatalytic water splitting, *Nat. Commun.* 8, 15341 (2017).
13. F. Ran, X. Xu, D. Pan, Y. Liu, Y. Bai, L. Shao, Ultrathin 2D Metal–Organic Framework Nanosheets In situ Interpenetrated by Functional CNTs for Hybrid Energy Storage Device, *Nano-Micro Lett.* 12(46) (2020).
14. Y. Song, X. Song, X. Wang, J. Bai, F. Cheng, C. Lin, X. Wang, H. Zhang, J. Sun, T. Zhao, H. Nara, Y. Sugahara, X. Li, Y. Yamauchi, Two-Dimensional Metal–Organic Framework Superstructures from Ice-Templated Self-Assembly, *J. Am. Chem. Soc.* 144(38) (2022) 17457–17467.
15. X. Fan, Y. Zhang, J. Li, K. Yang, Z. Liang, Y. Chen, C. Zhao, Z. Zhang, K. Mai, A general dissolution–recrystallization strategy to achieve sulfur-encapsulated carbon for an advanced lithium–sulfur battery, *J. Mater. Chem. A* 6(25), (2018) 11664–11669.
16. L. Zou, C.-C. Hou, Z. Liu, H. Pang, Q. Xu, Superlong single-crystal metal–organic framework nanotubes, *J. Am. Chem. Soc.* 140(45), (2018) 15393–15401.
17. D. Bi, N. Shen, Z. Tang, Z. Yang, S. A. Grigoriev, P. He, Q. Lai, Y. Liang, Defective carbon derived using a dissolution–recrystallization strategy for oxygen reduction electrocatalysis, *ACS Appl. Mater. Interfaces* 15(25), (2023) 30179–30186.
18. J. Luczak, M. Kroczewska, M. Baluk, J. Sowik, P. Mazierski, A. Zaleska-Medynska, Morphology control through the synthesis of metal-organic frameworks, *Adv. Colloid Interface Sci.* 314 (2023) 102864.
19. A. Schaate, P. Roy, A. Godt, J. Lippke, F. Waltz, M. Wiebcke, P. Behrens, Modulated Synthesis of Zr-Based Metal-Organic Frameworks: From Nano to Single Crystals, *Chem.-Eur. J.* 17(24) (2011) 6643-6651.
20. T. Tsuruoka, S. Furukawa, Y. Takashima, K. Yoshida, S. Isoda, S. Kitagawa, Nanoporous Nanorods Fabricated by Coordination Modulation and Oriented Attachment Growth, *Angew Chem. Int. Ed.* 48(26) (2009) 4739-4743.
21. W.X. Ge, Y.X. Chen, Y. Fan, Y.H. Zhu, H.L. Liu, L. Song, Z. Liu, C. Lian, H.L. Jiang, C.Z. Li, Dynamically Formed Surfactant Assembly at the Electrified Electrode-Electrolyte Interface Boosting CO Electroreduction, *J. Am. Chem. Soc.* 144(14) (2022) 6613-6622.
22. D.N. Jiang, C. Huang, J. Zhu, P. Wang, Z.M. Liu, D. Fang, Classification and role of modulators on crystal engineering of metal organic frameworks (MOFs), *Coordin. Chem. Rev.* 444 (2021) 214064.
23. J. Hwang, R. Yan, M. Oschatz, B.V. Schmidt, Solvent mediated morphology control of zinc MOFs as carbon templates for application in supercapacitors, *J. Mater. Chem. A* 6(46) (2018) 23521-23530.
24. X. Liu, H. Xie, J. Mao, Morphology-controlled synthesis of [LaFe(CN)6] and the porous erythrocyte-like

derivant applied for high-performance supercapacitors, *J. Electroanal. Chem.* 911 (2022) 116228.
25. Y. Niu, Y. Yuan, Q. Zhang, F. Chang, L. Yang, Z. Chen, Z. Bai, Morphology-controlled synthesis of metal-organic frameworks derived lattice plane-altered iron oxide for efficient trifunctional electrocatalysts, *Nano Energy* 82 (2021) 105699.
26. F.-B. Zhang, Z.-S. Fan, B. Yuliarto, S.M. Osman, M. Kim, Y. Yamauchi, Recrystallization strategy of ZnBTC nanowires and derivates for supercapacitor application, *Chem. Eng. J.* 486 (2024) 150112.
27. M. Liu, Z.M. Hudson, Macro-/mesoporous Metal-Organic Frameworks Templated by Amphiphilic Block Copolymers Enable Enhanced Uptake of Large Molecules, *Adv. Funct. Mater.* 33(26) (2023) 202214262.
28. D.H. Yang, T.T.T. Nguyen, S.T. Navale, L.H.T. Nguyen, Y.T. Dang, N.X.D. Mai, T.B. Phan, J.Y. Kim, T.L.H. Doan, S.S. Kim, H.W. Kim, Novel amine-functionalized zinc-based metal-organic framework for low-temperature chemiresistive hydrogen sensing, *Sensor Actuat. B-Chem.* 368 (2022) 132120.
29. J.Z. Chen, R.L. Liu, H. Gao, L.M. Chen, D.Q. Ye, Amine-functionalized metal-organic frameworks for the transesterification of triglycerides, *J. Mater. Chem. A* 2(20) (2014) 7205-7213.
30. K.-L. Zhang, H.-Y. Gao, N. Qiao, F. Zhou, G.-W. Diao, Preparation and characterization of two novel three-dimensional supramolecular networks with blue photoluminescence, *Inorg. Chim. Acta.* 361(1) (2008) 153-160.
31. J. Zhang, E. Hu, F. Liu, H. Li, T. Xia, Growth of robust metal–organic framework films by spontaneous oxidation of a metal substrate for NO2 sensing, *Mater. Chem. Front.* 5(17) (2021) 6476-6484.
32. E. Choi, P.M. Heynderickx, Solubility measurement and correlation of 2-aminoterephthalic acid in eight alcoholic solvents at different temperatures, *J. Chem. Thermodyn.* 177 (2023) 106948.
33. M. Bosch, M. Zhang, H.-C. Zhou, Increasing the Stability of Metal-Organic Frameworks, *Adv. Chem.* 2014(1) (2014) 182327.
34. W. Xue, Z. Zhang, H. Huang, C. Zhong, D. Mei, Theoretical Insights into the Initial Hydrolytic Breakdown of HKUST-1, *J. Phys. Chem. C* 124(3) (2020) 1991-2001.
35. M. Kim, H. Nara, Y. Asakura, T. Hamada, P. Yan, J. Earnshaw, M. An, M. Eguchi, Y. Yamauchi, End-to-End Pierced Carbon Nanosheets with Meso-Holes, *Adv. Sci.* 12(3) (2025) 2409546.
36. M. Kim, R. Xin, J. Earnshaw, J. Tang, J. P. Hill, A. Ashok, A. K. Nanjundan, J. Kim, C. Young, Y. Sugahara, J. Na, Y. Yamauchi, MOF-derived nanoporous carbons with diverse tunable nanoarchitectures, *Nat. Protoc.* 17 (2022) 2990-3027.
37. X.L. Zhang, J.F. Li, J.B. Li, L. Han, T. Lu, X.J. Zhang, G. Zhu, L.K. Pan, 3D TiO_2@nitrogen-doped carbon/Fe_7S_8 composite derived from polypyrrole-encapsulated alkalized MXene as anode material for high-

performance lithium-ion batteries, *Chem. Eng. J.* 385 (2020) 123394.

38. M. Ding, K.K.R. Bannuru, Y. Wang, L. Guo, A. Baji, H.Y. Yang, Free-Standing Electrodes Derived from Metal-Organic Frameworks/ Nanofibers Hybrids for Membrane Capacitive Deionization, *Adv. Mater. Technol.* 3(11) (2018) 201800135.

39. S.C. Tian, J. Wu, X.H. Zhang, K. Ostrikov, Z.H. Zhang, Capacitive deionization with nitrogen-doped highly ordered mesoporous carbon electrodes, *Chem. Eng. J.* 380 (2020) 122514.

40. E. Nightingale Jr, Phenomenological theory of ion solvation. Effective radii of hydrated ions, *J. Phys. Chem.* 63(9) (1959) 1381-1387.

41. D.A. Suwandi, E. Taer, R. Farma, R.F. Syahputra, Effect of aqueous electrolyte to the supercapacitor electrode performance made from sugar palm fronds waste, *J Phys.: Conf. Ser.* 1951(2021) 012009.

42. Z. Li, Z.W. Xu, X.H. Tan, H.L. Wang, C.M.B. Holt, T. Stephenson, B.C. Olsen, D. Mitlin, Mesoporous nitrogen-rich carbons derived from protein for ultra-high capacity battery anodes and supercapacitors, *Energy Environ. Sci.* 6(3) (2013) 871-878.

43. J.W. Jeon, S. Nune, J.L. Lutkenhaus, In situ one-step synthesis of hierarchical nitrogen-doped porous carbon for high performance supercapacitors, *ACS Appl. Mater. Interfaces* 6 (2014) 7214-7222.

44.Y. Song, L. Li, Y. Wang, C. Wang, Z. Guo and Y. Xia, *ChemPhysChem* 15 (2014) 2084-2093.

45.Y. Wang, Y. Song and Y. Xia, *Chem. Soc. Rev.* 45 (2016) 5925-5950.

46. M. Kim, L. Ma, Z. Li, W. Mai, N. Amiralian, A. E. Rowan, Y. Yamauchi, A. Qin, R. A. Afzal, D. Martin, A. K. Nanjundan, J. Li, N and S co-doped nanosheet-like porous carbon derived from sorghum biomass: mechanical nanoarchitecturing for upgraded potassium ion batteries, *J. Mater. Chem. A* 11 (2023) 16626-16635.

47. J. Liu, S. Webster, D.L. Carroll, Temperature and Flow Rate of NH3 Effects on Nitrogen Content and Doping Environments of Carbon Nanotubes Grown by Injection CVD Method, *J. Phys. Chem. B* 109(33) (2005) 15769-15774.

48. M. Eddaoudi, J. Kim, N. Rosi, D. Vodak, J. Wachter, M. O'Keeffe and O. M. Yaghi, *Science* 295 (2002) 469-472.

49. J. Yang, J. Meng, L. Zhang, K. Chu, W. Zong, L. Ge, S. Fu, J. Ge, H. Zhu, G. He, D.J.L. Brett, F. Lai, T. Liu, Dodecahedral carbon with hierarchical porous channels and bi-heteroatom modulated interface for high-performance symmetric supercapacitors, *J. Power Sources* 549 (2022) 232111.

50. Z.S. Fan, Y.V. Kaneti, S. Chowdhury, X.H. Wang, M.R. Karim, I.A. Alnaser, F.B. Zhang, Weak base-modulated synthesis of bundle-like carbon superstructures from metal-organic framework for high-

performance supercapacitors, *Chem. Eng. J.* 462 (2023) 142094.

51. F. Gao, J. Qu, C. Geng, G. Shao, M. Wu, Self-templating synthesis of nitrogen-decorated hierarchical porous carbon from shrimp shell for supercapacitors, *J. Mater. Chem. A* 4(19) (2016) 7445-7452.

52. B. Wang, Y. Li, Z. Gu, H. Wang, X. Liu, S. Li, X. Chen, X. Liang, Z. Jiang, K. Ogino, H. Si, Synthesis and design of biomass-derived heteroatom-doped hierarchical porous carbon systems for high-voltage supercapacitors, *Fuel Process Technol.* 247 (2023) 107776.

53. F. Sun, J. Gao, X. Pi, L. Wang, Y. Yang, Z. Qu, S. Wu, High performance aqueous supercapacitor based on highly nitrogen-doped carbon nanospheres with unimodal mesoporosity, *J. Power Sources* 337 (2017) 189-196.

54. Z. Ye, F. Wang, C. Jia, Z. Shao, Biomass-based O, N-codoped activated carbon aerogels with ultramicropores for supercapacitors, *J. Mater. Sci.* 53(17) (2018) 12374-12387.

Data Availability Statement

The data supporting this article have been included as part of the Supplementary Information.